J. Lewalle[1], M.Y. Ali[1], I.G. Boxx[2], K.P. Geigle[2], C.D. Carter[3]

[1] Department of Mechanical and Aerospace Engineering, Syracuse University
[2] Institute for Combustion Technology, The German Aerospace Center.
[3]Air Force Research Laboratory

"On the interactions of an axisymmetric and two precessing modes in a model combustor"

a.k.a.

"About an axisymmetric mode and a helical mode in the stable state of a model combustor"

Paper # AIAA 2018-1877

The AIAA version of the paper is accessible at
https://doi.org/10.2514/6.2018-1877

On the AIAA web page
https://arc.aiaa.org/doi/abs/10.2514/6.2018-1877
the interested reader can find other material published by AIAA

About an axisymmetric mode and a helical mode in the stable state of a model combustor

Jacques Lewalle[1] and Mohd Y. Ali[2]
Syracuse University

Isaac G. Boxx[3] and Klaus-Peter Geigle[4]
DLR Stuttgart

and

Campbell D. Carter[5]
Aerospace Systems Directorate, Air Force Research Laboroatory

3-component particle image velocitmetry data from a model swirl combustor are analyzed. Our previous work focused on the spontaneous transition from the stable state to the thermoacoustically excited state. Time-frequency (bandpass filterering) methods revealed a sequence of quasi-periodic modes, intermittent in time and in space. In this paper, we focus on the coexistence and interactions between two modes in the stable regime. The simplest is the axisymmetric mode, with vortex rings as the organizing flow structure. More complicated is the precessing mode, which combines a pair of counter-rotating helical vortices and a precessing recirculating vortex core. Using dynamic mode decomposition (DMD) yields different frequencies for the dominant modes. We reconcile the two methods by noting that DMD yields the fastest growing modes, whereas Fourier-related methods yield energy-dominant modes. We show that, on average, the growth of the helical or the axisymmetric mode precedes its peak energy by one to four periods. We also show that the mode amplitudes are correlated with varying signs across the burner.

I. Introduction and background

Swirling jets, confined or not, isothermal or with combustion, exhibit complex flow structures and dynamics. Early work on the stability of the vortex core (Sarpkaya[1], Leibovich[2]) put the spotlight on the balance of centrifugal forces and inertia in producing a recirculation zone on the vortex axis. They identified the swirl number as the critical parameter deciding on the formation of a recirculating vortex core. The break of symmetry associated with the presence of a helical mode, the effect of upstream conditions, the acoustic feedback, the existence of multiple flow patterns and the combination of combustion and compressible turbulence, all contribute to making the control of such flows more challenging.

The German Aerospace Center (Deutsches Zentrum für Luft- und Raumfahrt, DLR) has led an effort in recent years to bridge the gap between fundamental scientific studies of soot formation and system-level characterization of gas turbine combustors. This effort has focused on acquiring detailed measurements of a series of soot-generating flames in a generic, swirl-stabilized combustor at elevated pressure. These flames are designed to capture much of the complexity of a modern, swirl-stabilized gas turbine combustor, while maintaining excellent optical access for point- and planar laser measurements.

As part of this effort, Lammel et al.[20] (2007) applied laser-induced incandescence (LII) and coherent anti-Stokes Raman scattering (CARS) spectroscopy to quantify the effects of pressure, equivalence ratio and secondary

[1] Research Professor, Mechanical and Aerospace Engineering, Syracuse Univ., Syracuse NY 13244, AIAA Member.
[2] Assistant Professor, Mechanical and Aerospace Engineering, Syracuse Univ., Syracuse NY 13244, AIAA Member.
[3] Staff Scientist, Institute of Combustion Technology, Stuttgart, Germany, AIAA Associate Fellow .
[4] Staff Scientist, Institute of Combustion Technology, Stuttgart, Germany.
[5] Principal Aerospace Engineer, AFRL/RQHF, 1950 Fifth Street, Wright-Patterson AFB, AIAA Associate Fellow.

oxidation air on mean soot distribution in swirl-stabilized, sooting ethylene-air flames at pressures up to 9 bars and thermal loads up to 45 kW. Their results showed the highest soot concentrations were to be found in the lower part of the inner recirculation zone (IRZ) of the combustor, where residence times and local fluid temperatures are high. The combustor used by Lammel et al.[19] (2007) was based on the well-characterized DLR Dual-swirl Gas Turbine Model Combustor or "DS-burner" (Weigand et al.[18], 2006; Geigle et al.[23], 2011) applied LII, CARS and particle image velocimetry (PIV) in a similar combustor at atmospheric pressure and found that injection of secondary air downstream of the flame zone results in drastic changes to soot distribution in the combustor. Geigle et al.[24] (2014) extended these measurements (in a slightly modified burner geometry) to include flames at pressures up to 5 bars and observed that, in addition to pressure and global equivalence ratio, soot concentrations and distribution were sensitive to the ratio of air flow supplied to the inner- and outer swirl nozzles. Geigle et al.[26] (2015) applied simultaneous LII and planar laser-induced fluorescence of OH (OH-PLIF) to study the spatial correlation of soot and high temperature combustion products in these flames. Their results showed the addition of air downstream of the main flame zone resulted in secondary combustion zones that burn out the high soot concentrations previously observed in the IRZ or even prevent their formation in the first place.

These studies produced a rich database of experimental measurements on sooting swirl-stabilized flames in a gas turbine model combustor. This database, however, is limited to single-shot measurements which yield only mean and fluctuating quantities of interest. Soot formation, agglomeration and oxidation are highly dynamic processes, dependent upon multiple tightly coupled parameters. It is therefore of considerable interest to acquire time-resolved measurements of quantities such as velocity, soot distribution and reaction zone location. Furthermore, these studies have focused primarily upon fuel-rich flame conditions. Although this is certainly of key interest in understanding soot-dynamics, it has been observed that even (globally) lean flames can produce soot, particularly in regions such as the IRZ, where long-residence times exist.

Our recent work (SciTech2017[36], TurboExpo2017[37]) is based on high-bandwidth optical laser imaging from high pressure model burners. The geometry of the burner is intended to provide boundary conditions for LES calculations. In section II, we summarize the experimental geometry and operating conditions. In section III, local periodicity (in both time and space) is documented in the stable regime.

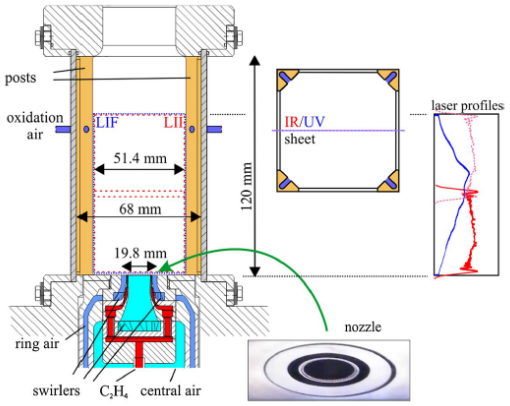

Figure 1: Schematic of the burner and data acquisition system.

A. Experimental conditions

This section is a summary of previously available information (e.g. SciTech2017[37]). The experiment consists of two major components; the burner, and the laser measurement system. Each component is described (separately) below.

Burner Configuration

The burner used in this study is of the same design as that described in Geigle et al.[26] (2015), see Fig. 1. It consists of a swirled fuel-air injector and a combustion chamber (with a square cross-section) mounted in an optically-accessible pressure housing. The swirled injector consists of a pair of coaxial nozzles, separated by a ring of fuel-injection channels. The inner nozzle is 12.3 mm in diameter. The outer (annular) nozzle has an inner and outer diameter of 14.4 and 19.8 mm, respectively. Air for the central and annular nozzles is supplied through separate pleni. Swirl is induced in each nozzle via a set of radial swirl vanes. Gaseous fuel (C_2H_4) is injected via a ring of 60 straight channels (0.5×0.4 mm^2) located between the central and the annular nozzles. This is designed to mimic the atomizing lip between swirled air flows in liquid-fuelled gas turbine injectors. The exit planes of the fuel and air flows are located at the level of the combustion chamber inlet (defined as height h = 0 mm), ensuring maximal optical access to flame dynamics at the nozzle exit.

The combustion chamber measures 120 mm in height and has a square section of 68×68 mm^2. Four quartz windows (127 mm × 59 mm × 3 mm) are mounted between four water-cooled metal posts yielding an optically-accessible area of 51.4 mm × 120 mm. The water-cooled top plate has a cylindrical contoured exhaust hole (diameter 40mm, length 24 mm), and is equipped with apressure transducer. Each of the four corner posts has an additional air duct of 5mm diameter for the injection of secondary air into the combustor at a height of 80 mm.

Although not used in the present study, the secondary air injection can be used to simulate combustor cooling or the effect of oxidation air on soot formation and agglomeration in the combustor.

The combustor is mounted in a water-cooled stainless steel pressure housing with four large windows for optical access (60×120 mm^2). The pressure inside the housing is adjusted by partially blocking the exhaust port with a movable piston. An air flow through the gap between the combustion chamber and the pressure housing serves as air cooling for the windows of the combustion chamber. The mean (inner) surface temperature of the windows is estimated to reach 773 – 1173 K during burner operation, depending on the position relative to the location of the flame. Although this is well below the melting point of the fused silica window material, the surface temperature is believed to fluctuate above the softening point of the material, dramatically increasing its susceptibility to particulate-fouling. This is a particularly challenging problem for imaging techniques such as PIV.

Flame Condition

Measurements in this study focused on single flow condition that produced a flame near stoichiometric, and had a 30/70 air split (30% of total air flow was injected through the center nozzle). A total of six long-duration measurement runs were acquired in this study. The flow parameters are summarized in Table 1.

Table 1 – Burner Operating Conditions

Condition	Pressure (Bars)	Stoichiometry	Thermal Load (kW)
1	5	0.98	54.2

Measurement System

The combined stereo-PIV/OH-PLIF measuring system used in this study has been described previously in the literature (Boxx et al.[24], 2010; Boxx et al.[28], 2014; Slabaugh et al.[37] 2016). As such, only a brief description of the PIV system is provided here.

Particle Image Velocimetry

The stereoscopic PIV system is based on a dual-cavity, diode-pumped, solid state Nd:YAG laser (Edgewave, IS200-2-LD) and a pair of CMOS cameras (LaVision HSS8). The laser produces a maximum of 9 mJ/pulse at 532 nm at a repetition rate up to 10 kHz. Pulse duration is approximately 10 ns. Pulse timing separation for the PIV system was $\Delta t = 10$ μs.

Three cylindrical lenses were used to form the laser sheet: f_{piv1}= -38 mm, f_{piv2} = 250mm, and f_{piv3} = 700 mm. To minimize noise arising from inter-frame particle dropout, the beam waist was located somewhat beyond the probe region. Mie scattering from titanium dioxide (TiO_2) particles (nominal diameter 0.5 μm) seeded into the air flow of each nozzle was imaged using a pair of CMOS cameras. The cameras were mounted on opposite sides of the laser sheet (at an angle looking "down" into the chamber) and had sufficient on-board memory (32 GB) for 3.8 seconds of continuous at 9300 Hz. For both PIV cameras, scattered light was collected with a 100-mm focal length, f/2.8 lens (Tokina) and image-blur due to off-axis defocusing was corrected using a Scheimpflug adaptor between the lens and camera. Perspective distortion was corrected using a dual-plane, three dimensional imaging target (LaVision Type 7). The same target was used to map the fields of view of the stereoscopic PIV and PLIF systems to one another. Image mapping, calibration, and particle cross-correlations were completed using a commercial, multi-pass adaptive window offset cross-correlation algorithm (LaVision DaVis 8.2). Final window size and overlap were 24×24 pixels and 50%, respectively. This corresponds to a spatial resolution of 2 mm and vector spacing of 1 mm. Based on the ±0.1 pixel uncertainty of the cross-correlation peak-finding algorithm, the random uncertainty of the PIV measurements is estimated to be ± 0.8 m/s.

B. Methods

To analyze the data, we use two complementary methods used previously in combustion research. Both methods rely on the decomposition of the field into building blocks, but they differ in the nature of these. First, wavelet methods belong with the Fourier group (band-pass filters, time-frequency representation), with time series as the elementary data; energy content organizes the results. Dynamic mode decomposition (DMD) is based on sequences of snapshots, and converge on the most active (rapidly growing) modes. Similarities and differences are both informative: the results will be described in Section II, and the discussion in Section III will reconcile them.

About continuous wavelet transforms

One of the data analysis tools used by our group is the continuous wavelet transform; as an alternative, we sometimes also use Fourier-based band-pass filtering. The relation between the two appears in the formulae listed in this subsection. We focus on continuous wavelets, because of the need to resolve frequencies to small fractions of octaves. A thorough presentation on continuous wavelets can be found in Mallat[7] (1998), while Lewalle, Farge & Schneider[18] (2007) provide an overview. The choice of a wavelet is governed by the desire to match the wavelet shape to the expected features of the signal. Because of the local periodicity observed in both stable and excited states, the Morlet wavelet (a complex Fourier wave under a Gaussian envelope) is our tool of choice. Our formulae differ from the standard presentation in three respects, as explained in Lewalle et al. 2007[18] and IGTI 2017 paper[37]. The Morlet wavelet includes two primary factors: a Fourier wave for which frequency is the only parameter, and a Gaussian envelope, which localizes the oscillation in time as a wave packet.

$$\psi(f,t) \sim \mathrm{e}^{-(2\pi ft/z_0)^2}(e^{-2i\pi ft} - e^{-z_0^2/2}).$$

The width of the envelope is proportional to z_0. In most commercial and online software, the default value of z_0 is 5, while larger values can be used when a better frequency resolution is desired (at the expense of time resolution). For this reason, the term $\exp(-z_0^2/2)$ is often negligible.

The wavelet normalization factor is defined as

$$c_\psi = \int |\hat{\psi}(f)|^2 \frac{df}{|f|},$$

where

$$\hat{\psi}(f) = \int \psi(t) e^{-2i\pi ft} dt$$

is the Fourier transform of ψ . Here, all time integrals extend over the entire real line. We note that there is no closed-form expression of c_ψ for the Morlet wavelet, which must be calculated numerically as a function of z_0. It is pre-calculated in our Matlab® functions and included in the definition of the wavelet itself, as follows. Our set for formulae consists of the Morlet wavelet

$$\psi(f,t) \sim \frac{f}{\sqrt{c_\psi}} \mathrm{e}^{-(2\pi ft/z_0)^2}(e^{-2i\pi ft} - e^{-z_0^2/2}),$$

the wavelet transform

$$\tilde{u}(f,t) = \int u(t')\psi^*(f, t-t')dt',$$

where the asterisk denotes the complex conjugate, the inverse transform

$$u(t) = \iint \tilde{u}(\mathrm{f},t')\psi(f,t-t')dt'\frac{df}{f},$$

and the Parseval theorem

$$\int |u(t)|^2 dt = \iint |\tilde{u}(f,t)|^2 dt \frac{df}{f}.$$

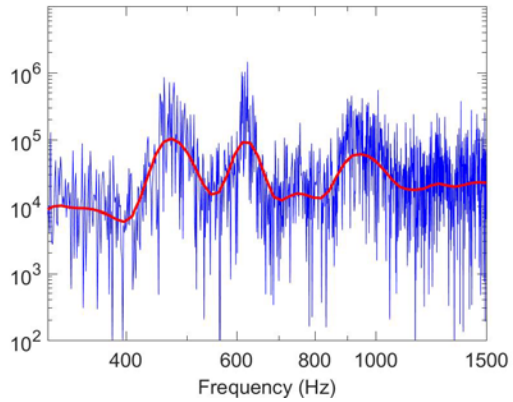

Figure 2: Compensated Fourier spectrum (blue) and its Morlet wavelet alternative (red).

The squared norm is proportional to the local energy content in time and frequency, as described by Parseval's formula and amounts to a smoothed Fourier spectrum, as illustrated in Fig. 2. We use compensated power spectra, i.e. power spectra multiplied by frequency. The spectra for axial component of velocity at one particular location show the agreement between the blue curve as the Fourier spectrum, the red curve the corresponding (smoother) Morlet wavelet spectrum. We identify local extrema of the spectrum (energy 'peak') at 473Hz, 620Hz, 750Hz, 945Hz (harmonic), 1261Hz (also harmonic). Frequencies vary slightly with location and with time, indicating both temporal and spatial intermittency and/or modulation, to be analyzed below. One of the advantages of wavelet processing is that time-averaging is not required: Parseval's theorem ensures that we can account for energy by adding contributions in time and frequency; this is captured by the scalograms (see below).

The norm of the Morlet coefficients can be interpreted as the envelope of the fluctuations at a given frequency, and the real part is a representation of the fluctuations inside the envelope. This is illustrated in Figure 3.

Finally, it should be noted that the wavelet transform can be interpreted as a band-pass filtered signal, with the weight of the Fourier modes dictated by the Fourier transform of the wavelet. Indeed,

$$\tilde{u}(f,t) = \int \hat{u}(\omega) e^{2i\pi\omega t} \hat{\psi}^*(\frac{\omega}{f}) d\omega$$

reduces to the inverse Fourier transform when $\hat{\psi} = 1$.

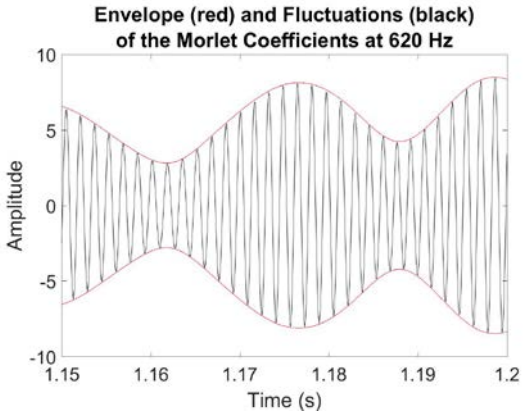

Figure 3: Illustration of a modulated oscillation and its envelope (from IGTI[23]).

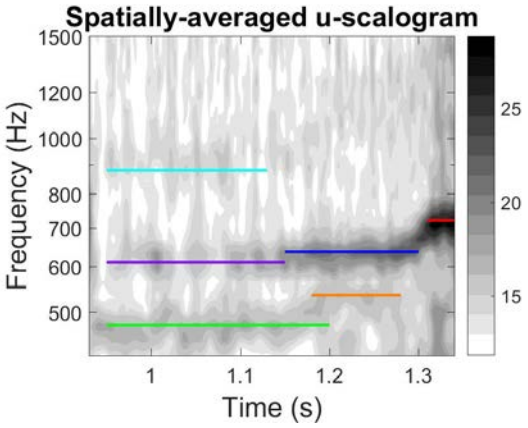

Figure 5: Example of a scalogram showing locally-periodic modes before, during and after transition from stable to excited state.

Previous work (SciTech201722, IGTI201723) documented some of the phenomena associated with the transition from a 'stable' to a thermoacoustically excited state. The usefulness of time-frequency methods is this context is illustrated in Fig. 5. With some spatial averaging to improve the signal to noise ratio, the norm of the Morlet wavelet coefficients is plotted in grey shades, with darker shades being more energetic. The stable state (t < 1.15s for this record) is characterized by the presence of two frequencies (475 and 620Hz) where intermittent (and spatially non-homogeneous) wave packets dominate the ambient random fluctuations. At the onset of transition, the 475Hz mode switches to 535Hz, and the 620Hz mode switches to 635Hz. After transition, a thermoacoustic mode at 720Hz dominates the excited state.

In this paper, we examine in more detail the coexistence between two of these modes in the stable state. The two modes are a 610-635Hz (with fluctuations in frequency as well as modulation in intensity) axisymmetric mode, characterized by vortex rings in the the jet's shear layers and axial oscillations downstream of the IRZ; and a 475Hz precessing mode, which combines the precessing IRZ and a pair of counter-rotating precessing helical vortices as the primary shear layer structures. The signals in the stable state are statistically stationary, but the intensity and even the frequency of the wave packets is far from constant. The frequencies listed above should be considered as merely nominal, for reference purposes.

About the dynamic mode decomposition (DMD)

The temporal DMD algorithm used in the present work was adapted from Schmid[23] (2010). The data set to be analyzed is time-resolved velocity field. A temporal sequence of N velocity fields (u and v components) is ordered into column vectors ($\mathbf{v}_j$) that are equispaced in time. The primary basis of the method is that each flowfield in time, is connected to a subsequent flowfield, ($\mathbf{v}_{j+1}$), by a linear mapping $\mathbf{A}$, such that, $\mathbf{v}_{j+1} = \mathbf{A}\,\mathbf{v}_j$. The eigenvalues and eigenvectors of the matrix $\mathbf{A}$ characterize the behavior of the dynamical system. The assumption of constant mapping of the dynamical system, $\mathbf{A}$, between the flowfield sequence allows us to formulate a Krylov sequence of the data (Schmid[23] (2010)). As the number of flowfields increase, the data set is assumed to approach a linear dependency. The last flowfield vector, $\mathbf{v}_N$, can be expressed as a linear combination of the previous linearly independent vectors,

$$\boldsymbol{v}_N = \boldsymbol{V}_1^{N-1}\boldsymbol{a} + \boldsymbol{r}$$

where **r** is the residual vector and the coefficient $\mathbf{a}^T$ can be obtained using the least squares method. Following Ruhe[3] (1984), the flowfield vector can be written as follows in the matrix form:

$$\boldsymbol{A}\boldsymbol{V}_1^{N-1} = \boldsymbol{V}_2^N = \boldsymbol{V}_1^{N-1}\boldsymbol{S} + \boldsymbol{r}\boldsymbol{e}_{N-1}^T$$

where $\mathbf{e}_{N-1}$ is the $(N-1)^{\text{th}}$ unit vector. The matrix **S** is of the companion type, which shifts the dataset (flowfield sequence) index from 1 to *N*-1. The number of flowfields, *N*, can be increased until the residual, **r**, converges. The matrix **S** is a low-dimensional representation of the the full system matrix **A**. The eigenvalues (λ_j) of matrix **S** approximate some of the eigenvalues of the full system matrix **A** (Schmid[23] (2010)), and are also referred to as the Ritz values (Rowley *et al.*[22] (2009)). The companion matrix **S** is computed by calculating the singular value decomposition of the flowfield matrix $\boldsymbol{V}_1^{N-1}$ and the approximate 'full' matrix,

$$\tilde{S} = U^H V_2^N W \Sigma^{-1} = U^H A U$$

which is obtained by projecting **A** on to **U**. The matrix **U** contains the POD basis and forms the right singular vector of the snapshot matrix $\boldsymbol{V}_1^{N-1}$. The eigenvalue decomposition of the matrix $\tilde{S}$ gives the eigenvalues, λ_j, and eigenvectors, $\boldsymbol{y}_j$, such that $\tilde{S}y_j = \lambda_j y_j$. Finally, the dynamic modes are computed as:

$$\Phi_j = U y_j$$

The approximate eigenvalues (Ritz values), λ_j , occur as complex conjugate pairs and lie on a unit circle in the complex domain. Furthermore, the eigenvalues can be mapped logarithmically as, $\omega_j = \log(\lambda_j)/\Delta t$, where $\Delta t = f_s^{-1}$ is the separation time between successive snapshots. The discrete frequencies of the decomposed data, f_j, are determined from the imaginary part of the logarithmically mapped eigenvalues as $f_j = 2\pi \,\mathrm{Im}\{\omega_j\} = \arg(\lambda_j)/(2\pi\Delta t)$. The negative frequencies are neglected and each mode pair is identified by the positive-valued frequency. The mean feature is a special case of DMD with zero eigenvalue (frequency), indicating that it is invariant in time. Beyond the zero-frequency case, the DMD-derived modes can be sorted by their amplitudes, $||\Phi||$.

DMD was successfully applied to swirling flows by Luginsland et al[27]. In this project, it was applied to the time resolved velocity data (axial *u* and radial *v* components) to identify any key structures in the flowfield. A total of 8192 velocity fields were used. The sampling frequency was 9300 Hz. The frequency spectra in Fig. 4 shows the mean frequency and peaks ar 430 Hz and 580 Hz. These correspond to the the most active, i.e. most rapidly growing modes. Other peaks fit a trend of larger values at decreasing frequencies, presumably associated with incomplete statistical convergence, and we do not study them here. The obvious question about the relation of the peak frequencies to the 475 and 620 Hz energy peak noted in the previous subsection, will be addressed below.

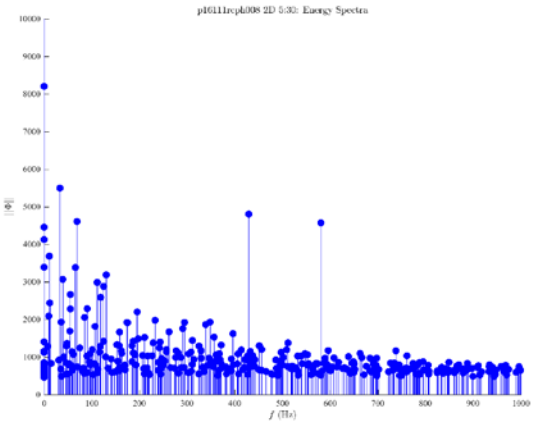

Figure 4: Frequency spectra from DMD analysis showing peaks at 430 Hz and 580 Hz.

II. Quasi-periodic flow structures

Before we turn to the temporal modulation, the spatially non-homogeneous distribution of the wave packets is documented. In Fig. 6, we plot the compensated spectra as functions of frequency and spanwise location, for various axial locations. The two main frequency peaks at 475 and 620 Hz are not present homogeneously in the burner, or equally between components. Following the flow direction upward from the nozzle, we see strong axial fluctuations are both frequencies, primarily in the inner shear layer; radial fluctuations are initially weak and span the core region at 475 Hz, but the 620 Hz radial peak is well developed by x ~ 12 mm, particularly in the outer part of the jet. By x ~ 17mm, the main change is the strengthening of the 475 Hz layer across the core -10 < y < 10 mm. We will associate this with the precessing vortex core later in this paper. For x > 20 mm, both components are generally strongest along the sides of the burner, however the main feature is the 625 Hz energetic line across the span for the axial component only: this may be interpreted as an axial oscillation, possibly thermoacoustic in association with the

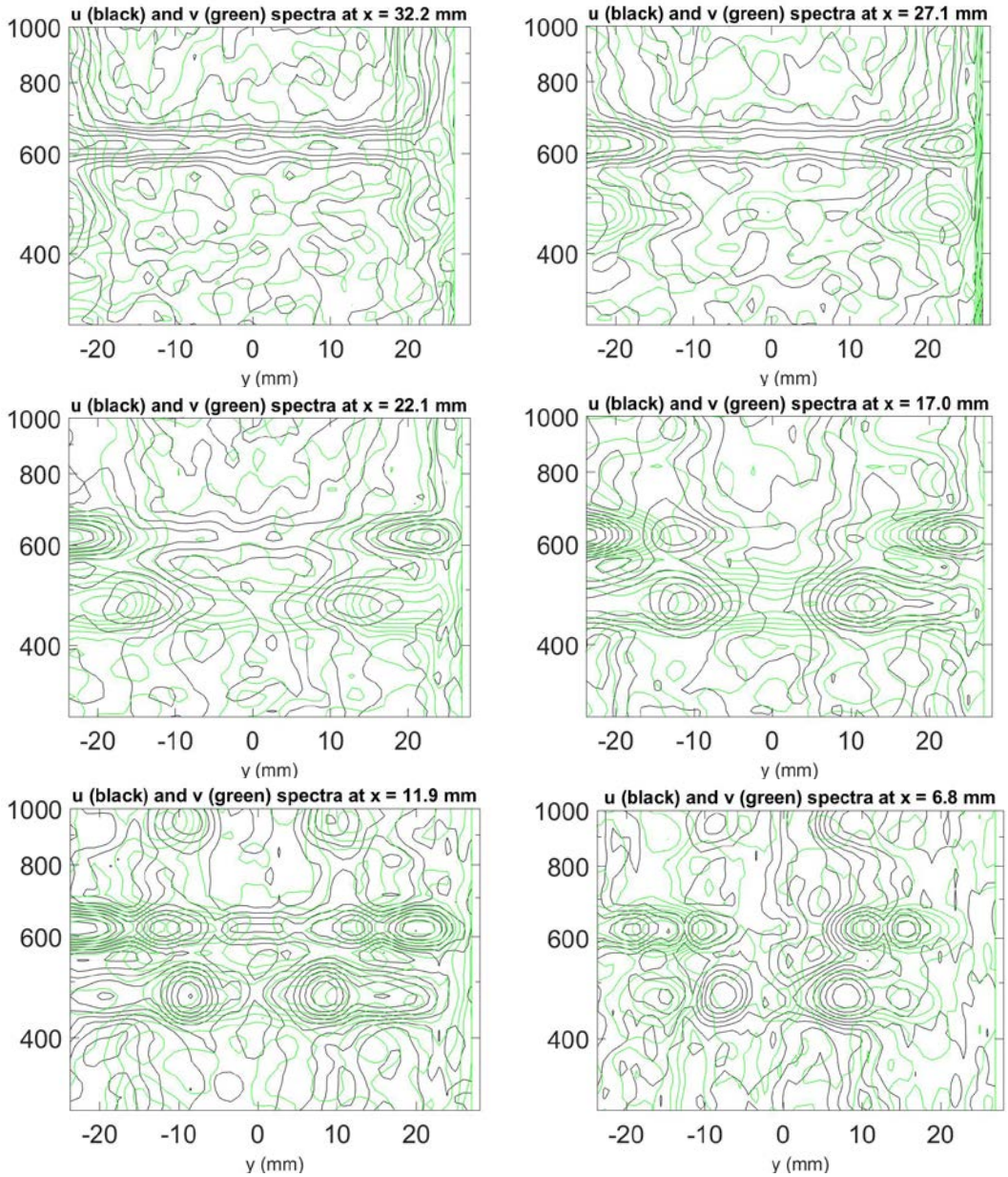

Figure 6: spanwise distribution of compensated Morlet spectra for the u and v components, at various axial locations.

exhaust viewed as a Helmholtz resonator.

We now proceed to analyze these two modes in greater detail. As in SciTech2017[36] and TurboExpo2017[37], we isolate the locally periodic modes by band-pass filtering the velocity signals in a 20 Hz band straddling the nominal frequency. In the papers just cited, we mapped out some properties of these 3-dimensional oscillations. We now continue this study for the stable state and the two dominant modes. Then we repeat the analysis for the corresponding DMD-dominant modes.

A. The precessing 475Hz mode

The band-pass filtered signals map the three components of velocity across the x-y PIV plane. We visualized the v-w components (in planes perpendicular to the burner's axis) by flipping them into the x-y plane (so the azimuthal component w appears as an axial component). We also calculated the azimuthal vorticity component associated with the u and v components of velocity. The result is shown in Fig. 7.

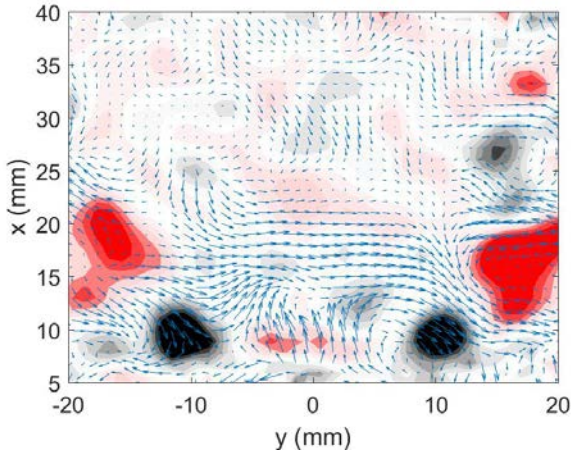

Figure 7: Azimuthal instantaneous vorticity distribution (red/black), and the corresponding v-w velocity vectors (flipped into the y-x plane) highlighting the IRZ and other out-of-plane motion.

A few features are noted. First, the azimuthal vorticity is concentrated in vortex cores of alternating signs in the outer shear layer. However, as noted in TurboExpo2017[37], the two black cores cannot be part of the same vortex, since the sign of azimuthal vorticity of a vortex ring would appear antisymmetric (see the 620 Hz mode, below). Therefore, they correspond to a pair of counterrotating helical vortices. Furthermore, as animated movies of such plots indicated, the v-w velocity appears nearly uniform over a core region extending roughly from $-10 < y < 10$ mm and $15 < x < 22$ mm. Within this region, the velocity vectors (actually in the horizontal plane perpendicular to the axis) appear to rotate once every cycle. One interpretation for the cycle of uniform velocity vectors rotating together is of a rigid body translating (not rotating appreciably) in a horizontal circular path. Thus, we associate the IRZ with the precessing vortex core (PVC). The precessing helical vortices (PHV's) are distinct flow structure. This seems qualitatively consistent with recent POD results from Markovich's group (Figs. 8 and 9), except for the counter-rotating helical pair, tentatively attributed to the distinctive nozzle in our experiment.

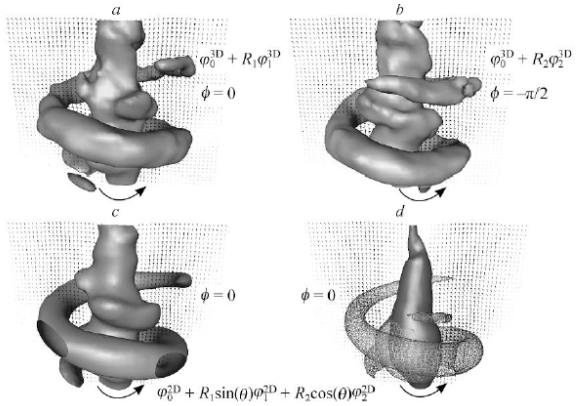

Figure 8: Helical vortex and vortex core, from Alekseenko et al, 2016;

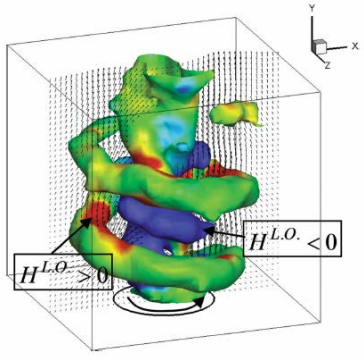

Figure 11. The low-order reconstruction of coherent structures in high-swirl jet ($S = 1.0$), based on POD of 3D velocity fields.

Figure 9: Helical vortex and vortex core, from Markovich et al., 2016

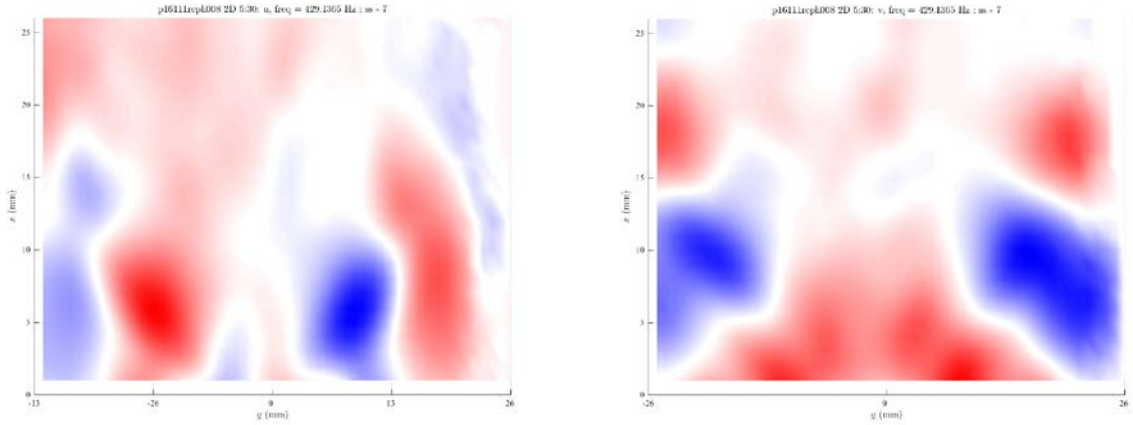

Figure 10: Real part of the axial and radial DMD eigenfunctions corresponding to 430 Hz.

The DMD mode corresponding to the helical vortex is associated with a lower frequency (430 rather than 475 Hz). It occupies the outer shear layer of the swirling jet, as seen in Fig. 10.

We proceeded with the characterization of the precession and its correlation with the PHV's. The v-w velocity vectors, distributed at the x-y PIV data points, were characterized by their oritentation in the y-z plane (angle relative to the y axis) and their magnitudes. First, we calculated an average angle within the IRZ; then we eliminated all mesh points where the velocity angle differred from the IRZ average by more than $\pi/6$, or of which the magnitude was less than 60% of the IRZ average. Then we retained only the contiguous patches of points containing at least 40 points. Two representative snapshots are shown in Fig. 11. The patch of coordinated horizontal velocities generally exhibits a slanted shape, presumably matching the pitch of the HVC. During part of the cycle, the patch is divided into two regions.

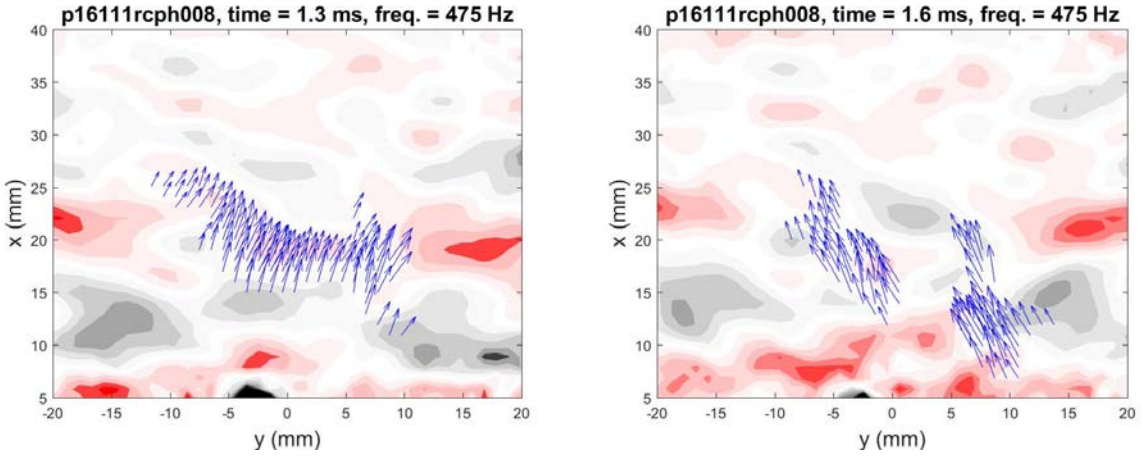

Figure 11: Two snapshots of the instantaneous vorticity distribution (red/black) and of the nearly-uniform horizontal motion, consistent with rigid-body translation in a circle (precession) by the recirculating IRZ; the precession velocity arrows have been flipped from the y-z plane to the y-x plane, originating from the correct (y,x) coordinate..

We note in passing that 'precessing vortex core' has been used with at least two different meanings by various authors. The original concept arose in the study of a confined vortex filament (Sarpkaya[1], Leibovich[2]16), and by extension to the recirculation zone around which the filament bifurcates. In the current configuration, this is consistent with the inner recirculation zone. The inner recirculation zone in our burner seems consistent with the original meaning. The near-rigid-body motion of this flow structure does not make it a Lagrangian structure, since

the flow circulates through it. But the precession of this structure must affect the shedding of vortices from the nozzle lips, resulting in the asymmetric and also precessing helical vortex. The large vorticity at the core of the helical vortex or vortices has led other authors to associate 'precessing vortex core' with the helical structures.

B. The axisymmetric 625 Hz mode

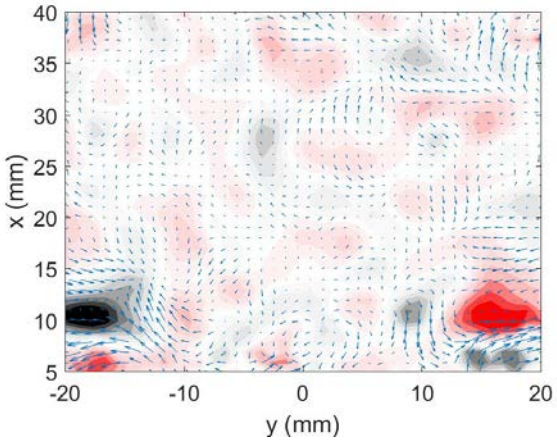

Figure 12: The axisymmetric mode, to be compared with Fig. 7.

In contrast, the 620 Hz mode shows velocity in the planes perpendicular to the burner axis to be negligible except in the outer recirculation zone (ORZ) (Fig. 12). The azimuthal component of vorticity is also propagating through the ORZ, with the antisymmetric configuration of the vortex cores consistent with axisymmetric vortex rings. The same location is observed for the DMD mode corresponding to 580 Hz, as seen in Fig. 13.

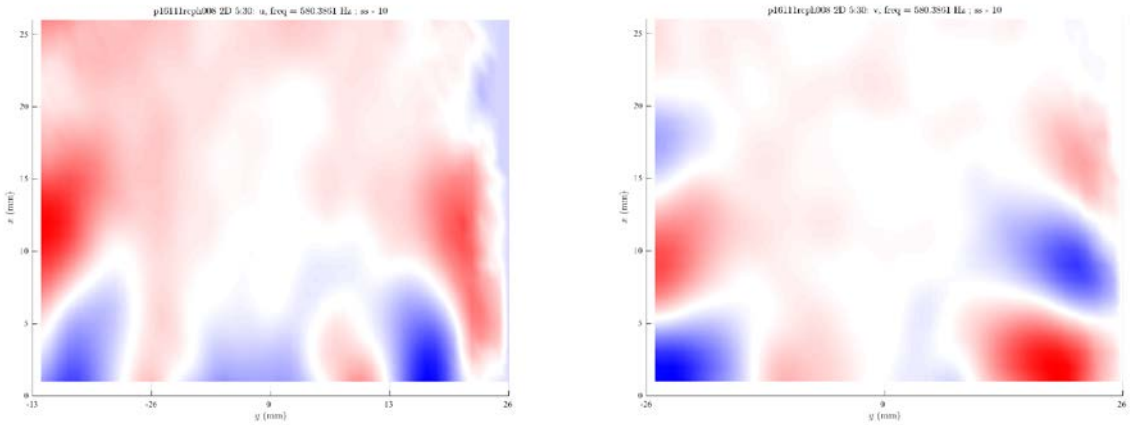

Figure 13: Real part of the axial and radial DMD eigenfunctions corresponding to 580 Hz.

The modal reconstruction of the field is illustrated in Table 2. Movies have been produced of the azimuthal vorticity associated with the filtered velocity, and snapshot (Fig. 14) illustrates the general agreement and noteworthy differences between the Fourier and DMD approaches. Both methods capture periodic vortices propagating along the jet's outer shear layer. The DMD vortices are smoother in appearance, which is attributed to the combination of whole-field treatment and convergence in time, whereas the Fourier approach treats signals locally (also over all time). The same reasoning applies to the 'noisy' exhaust and outer recirculation regions in the Fourier case. Also noteworthy is the strong (counter-rotating) vortex in the inner shear layer captured by the Fourier filter but not by DMD, implying that inner layer is not associated with growing fluctuations. Two discrepancies about the DMD filtering were not resolved at the time of writing: a blinking in the intensity of the field, and small backward steps by the vortices. We comment on them in section III.

Real field u(x,y,t)	**Fourier**	**DMD**
Complex Mode	$F_f(t) = \exp(i\, f\, t)$	$M_f(x,y)$
Coefficients	$\mathcal{U}_f(x,y,f) = \mathrm{Sum}_t\,(F_f^* \cdot u(t))$	$\mathcal{U}_f(t) = \mathrm{Sum}_{x,y}\,(M_f^* \cdot u)$
Filtered field	$U(x,y,t) = \mathrm{Real}(\mathrm{Sum}_f\, \mathcal{U}_f(x,y,f)\, F_f)$	$U(x,y,t) = \mathrm{Real}(\mathrm{Sum}_f\, \mathcal{U}_f(t)\, M_f(x,y))$

Table 2: Similarity of Fourier and DMD filtering formulae; * denotes complex conjugation, the DMD modes are labeled according to frequency for simplificy, the Sums apply to the desired time, space or frequency range.

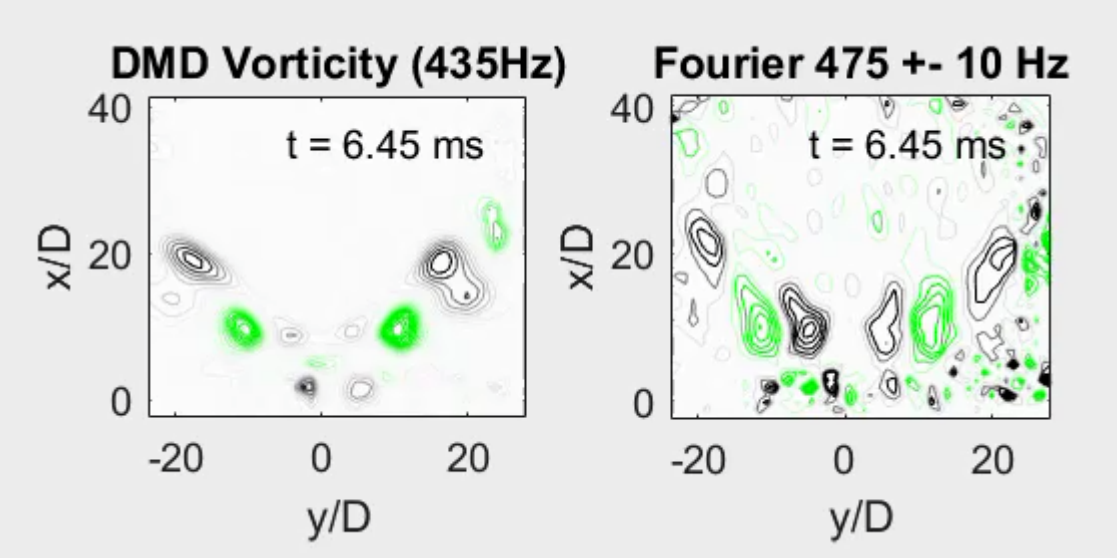

Figure 14: Vorticity snapshot in DMD- and Fourier-filtered fields.

C. Interactions between modes

We now look at correlations between the helical vortex cores and the precessing IRZ, and at interactions between the precessing structures and the axisymmetric mode. We focus on the envelope of the fluctuations, to capture the correlations of *modulation* of the oscillations. Among our hypotheses are that they could be symbiotic (positively correlated), in competition with each other (negatively correlated) or indifferent. However, correlations would not be simply at one point, since the flow structures inhabit different regions of the burner.

Therefore, we constructed the space-time cross-correlations of the envelopes of the signals (Kan[41]). We select a reference point, component and modal frequency, and cross-correlate the entire field, possibly of another component and at another frequency, with lags spanning many cycles of the reference oscillation. Movies of such correlations will be shown. Here we show one representative figure of the correlation (zero lag) between the radial components (both at 475 Hz) at zero lag. The large patch of positive correlation (Fig. 15) around the reference point in the IRZ shows that the helical vortices are strongest when the IRZ precession is strongest.

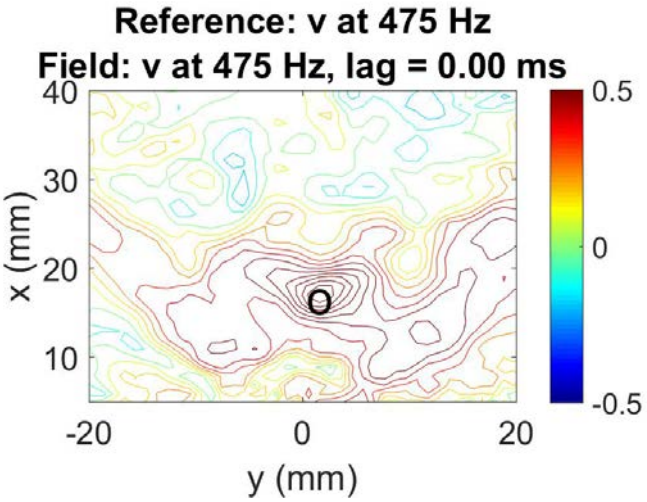

Figure 15: Correlation coefficient between the envelopes of the 475Hz radial oscillation at the reference points (marked by O) and the rest of the field.

Looking next at the interactions between modes (Fig. 16), we take the 625Hz axial component in upper part of the burner as the reference signal, and correlate its envelope to the envelopes of the 475 precessing u and v compoents. At zero lag, we see that the radial component at 475 Hz in the IRZ is negatively correlated with the reference signal, indicating the precession is weaker when the axial oscillations are strongest. This is consistent with axial oscillations being axisymmetric, whereas the helical mode is asymmetric. On the other hand, the correlation of the axial envelope with itself, both at 625 Hz, shows strong positive correlation in the entire field except in the IRZ, where the axial component seems to be indifferent to the strength of the axisymmetric mode. Movies show the dependence of the correlation patterns with lag (relative to the reference signal).

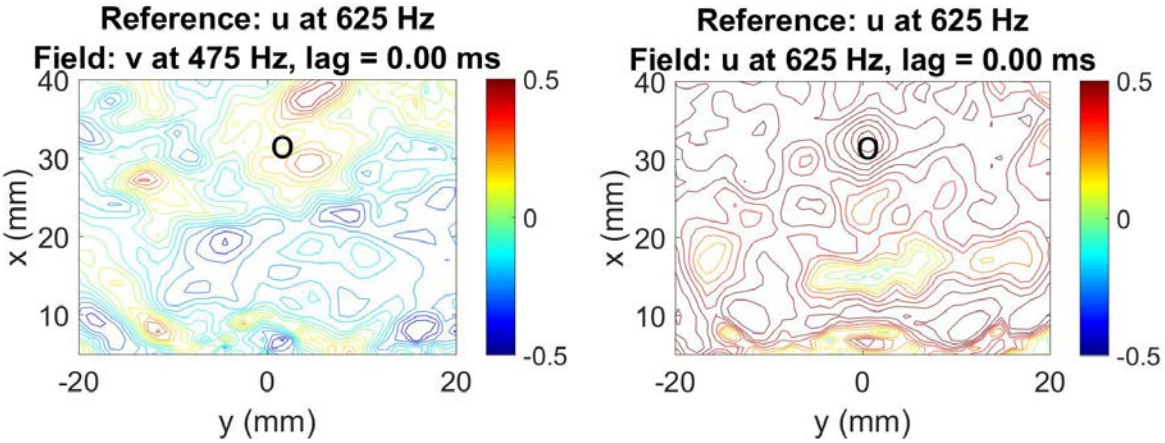

Figure 16: Correlation coefficient between the envelopes of 625Hz axial fluctuations and the rest of the field, as labeled.

Growing modes vs. energy-containing modes

Frequency-dependent growth rate in the Fourier/wavelet representation is based on the envelopes of fluctuations within successive wavepackets. Regardless of preliminary Fourier band-pass filtering, the envelope (modulated magnitude) is calculated as the norm of the Morlet coefficients. In this section, the scalograms are averaged in groups of 3 axial and 3 radial points surrounding their nominal location, in order to improve the signal-to-noise ratio (SciTech17[42]). Given the coefficients at a given frequency, a dimensionless growth rate is calculated as the mean slope of the coefficients (normalized by their local standard deviation), in time (multiplied by frequency). The time averaging is conditioned on the slope being positive, capturing mean growth rates.

In the vicinity of 475 Hz, the result at a representative point is shown in Fig 17. For either u or v, we see that the energy-dominant frequency is associated with the smallest average growth rate. The spatial distribution of the mean growth rate curves is shown in Fig. 18. With a few exceptions, we see that the convex shape is observed at most locations for one or the other velocity component, only along the side wall are consistent departures observed for both u and v. Along the burner axis, the u component does not exhibit the convex growth rate vs frequency, whereas v does.

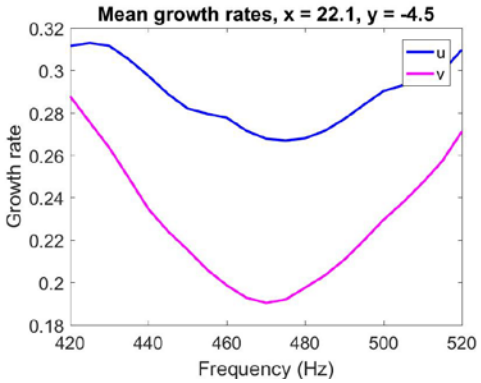

Figure 17: dimensionless mean growth rate as function of frequency

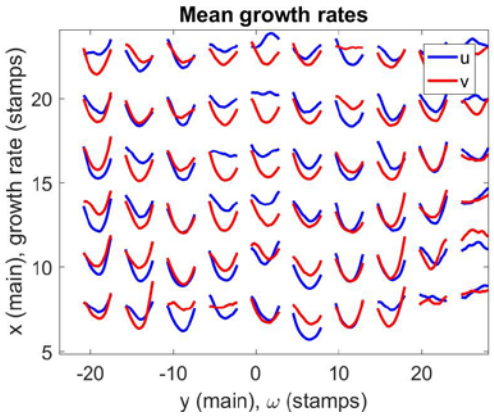

Figure 18: Spatial distribution of growth rates

The convex shape of the growth rates near the energy-dominant helical mode does not explain why the DMD frequency is 430 Hz, rather than a value larger than 475Hz. For an answer to this question, we superposed the scalograms of Morlet-norm-squared coefficients (contour lines) and the corresponding growth rates (positive values in grey shades), as shown in Fig. 19. We see that, for the sequence of wave packets shown here, each new packet is preceded by a more intense growth rate at a higher or lower frequency. This is more obvious for the u component for this particular excerpt.

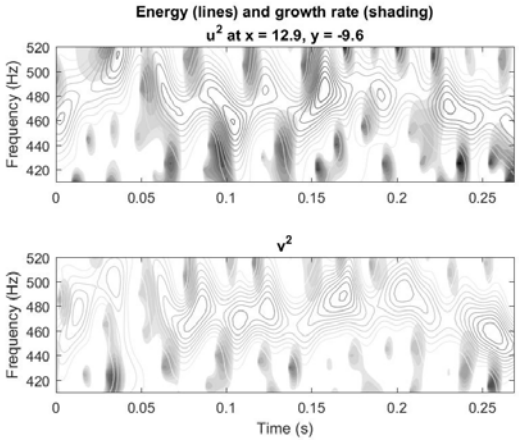

Figure 19: time-frequency excerpts of energy density (contour lines) and growth rate (shades of grey) for u (top) and v (bottom)

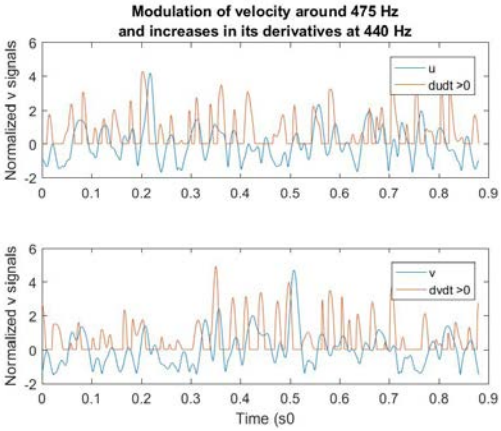

Figure 20: traces of normalized filtered velocities (blue) and truncated growth rates (red)

The next question is then whether the most active (DMD) mode at 430Hz could be, in a statistical sense, a precursor of the energy-dominant wave packets (Parseval) at 475Hz. One way to establish a precursor is to cross-correlate the growth rate (truncated to keep only positive slopes) around 430Hz and the energy density around 475Hz. Typical signals of these types are illustrated in Fig 20.

For our relatively short signals, background correlation coefficients associated with incomplete statistical convergence are in the (-0.2,+0.2) range, with a standard deviation of about 0.15. The cross-correlations exhibit fluctuations meeting this description, with a significantly larger positive peak at small positive lags. Several

examples of the short-lag cross-correlations are shown in Figs. 21 (475Hz) and 23 (610Hz). The lags are made dimensionless using the nominal Fourier frequency; therefore, the peak lags in the range of 2 to 4 units indicate that the precursor at 430Hz (580Hz) trigger the dominant mode within as few cycles.
The spatial distribution of the precursor effect is shown in Figs. 22 and 24. At the 0.4 threshold for the helical mode (475Hz), the precursor effect is seen only along the axis, along the side wall of the burner and in the ORZ, specifically excluding the jet region. The 610Hz (axisymmetric) correlation peaks are stronger. In this case, only the jet region does not reach the threshold.

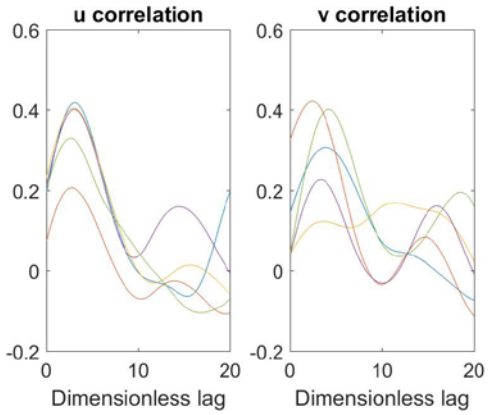

Figure 21: Cross-correlation of 430Hz growth rate and 475Hz energy density

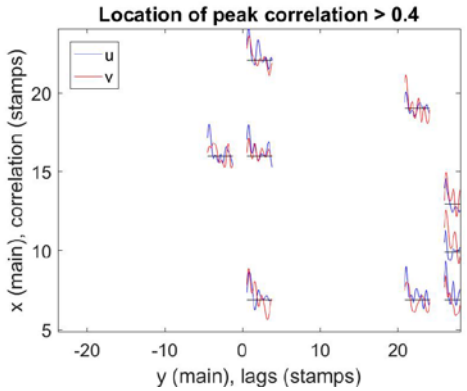

Figure 22: Spatial distribution of strong correlation indicating the growth of the 430Hz leading to energetic 475Hz wave packets (precursor effect).

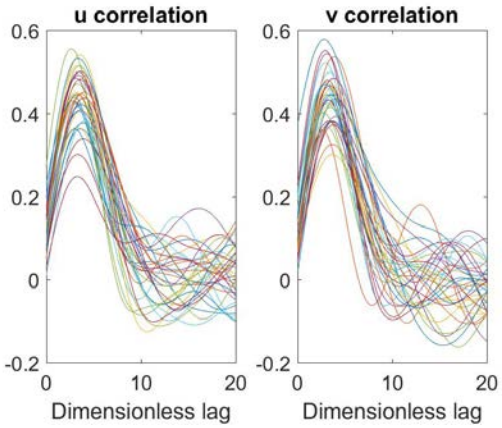

Figure 23: Cross-correlation of 580Hz growth rate and 610Hz energy density

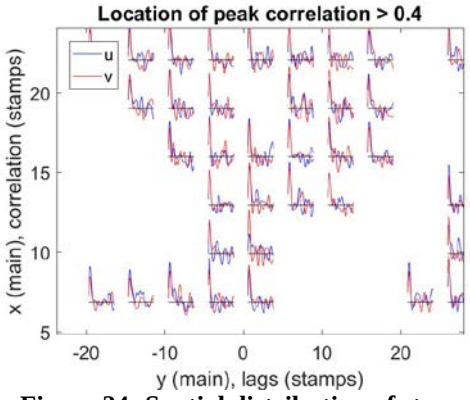

Figure 24: Spatial distribution of strong correlation indicating the growth of the 580Hz leading to energetic 610Hz wave packets (precursor effect).

III. Discussion and on-going work

Building on earlier work[30,31], this paper focuses on the stable state of the model swirl-stabilized combustor. In this state, two types of quasi-periodic flow structures stand out from the turbulent background. The frequencies of these vortical structures vary in time, and the values adopted to describe them (475Hz and 610Hz) should be understood as being merely nominal; their amplitudes are also time dependent. We can think of them as modulated in frequency and amplitude. These structures do not fill the entire space of the combustor: they are active in specific regions. In this regard, the 610Hz structures are simpler, in that they consist of vortex rings propagating downstream on the outside of the swirling jet. Slightly inward of these axisymmetric vortices are counter-rotating pairs of helical vortices at the 475Hz nominal frequency. The question remains open whether the helical vortices coexist, compete

or interact with the vortex rings. The helical vortices are precessing about the burner's axis; their inherent asymmetry induces a corresponding asymmetry of the core of the flow, detectable in the inner recirculation zone, with corresponding precession. Consistently with the Biot-Savart relation, induced motion does not imply a cause-and-effect relation: the helical vortex and the off-center IRZ cannot exist independently of each other.

Several methods document complementary aspects of the quasi-periodic flow structures. In previous work, we used continuous wavelets (time-frequency) tools, and related Fourier band-pass filtering, to process time-series extracted at each point from the sequence of PIV frames. The focus in this context is on the Parseval theorem (and on energetic fluctuations) and on cross-correlations between signals to track the propagation of fluctuations. Because of the limited duration of the signals, this approach must accommodate incomplete statistical convergence of power spectra and correlations. Over the past 10 years, dynamic mode decomposition (DMD), related to Koopman operators, has provided an alternative to the classical proper orthogonal decomposition (POD). Like POD, DMD is well suited to the treatment of arrays (such as PIV or LES results) arranged in a sequence. DMD is distinctive for its emphasis, not on the energy-containing modes, but on the rapidly-growing (most active) modes. This distinction makes it well suited for flow control applications. Just as in POD, a sequence of complex eigenfunctions, and corresponding eigenvalues, can serve as a the basis functions to reconstruct the flow; retaining a selection of modes in the reconstruction is one potentially useful filtering approach.

The whole-field treatment in DMD is not necessarily well suited to the analysis of non-homogeneous flow fields with different flow structures in different regions. Treating the entire axial range yielded only the 435Hz (nominal) mode, with no clear activity in the IRZ, whereas limiting the field to $5 < x < 25$ mm added the 580 Hz mode. Further refinements need to be carried out, given the partitioning of the flow in this burner into multiple regions with distinctive flow structures and dynamics. The current selection ($5 < x < 25$ mm) allowed us to compare the Fourier-based and DMD-based results for the helical and axisymmetric modes. The anomalous evolution of the DMD-based filtering of the field will be addressed in the future.

The apparent discrepancy between the Fourier- and DMD-frequencies is resolved by considering that the former identifies the energetic modes, whereas the latter identifies the growing modes. In view of the similarity in flow patterns, we explored the possible sequence of e.g. a helical mode growing from 435 Hz to settle at the peak energy of 475 Hz; and similarly the vortex ring mode growing from 580 Hz to peak energy around 610 Hz. While we found no direct evidence for such a sequence, its statistical footprint, in the cross-correlation between the envelopes of growing mode and of the energetic modes shows a strong peak at a lag of about 3 periods of the respective wave packets.

The coexistence of the helical mode and the precessing IRZ is noted, and seemingly unavoidable for reasons of symmetry and kinematic constraints (Biot-Savart). We characterized the precessing IRZ as a flow region translating in circular horizontal motion as a rigid body, through which the motion of the recirculating fluid is not detectable in the range of the precessing frequency. The break-up and recombination of the precessing IRZ maybe an artifact of the frequency filtering. Extending this analysis to the DMD modes implies the use of the azimuthal component of velocity, and is part of on-going work. However, we noted that the single-mode DMD-filtered velocity (Fig. 14) has questionable properties; at the time of writing, a simple one-dimensional model shows that this can be due to an interplay of discretization (in time and space), of the growing stage frequency (and wavelength) being imposed on the longer-lived peak-energy frequency, and on ambient noise. This is work in progress.

Just as for the transition, where we showed (IGTI[17]) the precursors to originate in the ORZ, the fluctuations in the ORZ seem to be associated with the growth of the axisymmetric and of the helical modes in the stable state. Therefore, the ORZ may be the region where flow actuation may yield the most effective control, if its environment were less hostile.

Interactions between the helical and the axisymmetric modes can be approached in two complementary ways. A mechanistic approach would look for times of activity or one versus the other, and compare them. This was unproductive, possibly because of the combination of spatial non-homogeneity and strong temporal modulation. The statistical approach was more productive, as the cross-correlation of envelopes of signals. It makes sense that 475Hz signals would, in that sense, be correlated to each other; it is far less obvious that 475Hz envelopes and 610Hz envelopes would be correlated, let alone with coefficients approaching 0.5 (positive and negative). The corresponding movies will be shown at the conference. We have only scratched the surface in this context: the selection of reference point and signal type, and all the corresponding fields, will be on the the front burner for the continuation of this project.

Acknowledgments

This material is based upon work supported by the Air Force Office of Scientific Research, Air Force Material Command, USAF under Award No. FA9550-16-1-0044.

C. Carter is supported under the Air Force *Windows on the World* program.

References

REFERENCES

[1] Sarpkaya, T, 1971, Vortex breakdown in swirling conical flows, AIAA J. 9/9, 1792-1799.
[2] Leibovich, S., 1978, The structure of vortex breakdown, Annu. Rev. Fluid Mech. 10, 221-246.
[3] Ruhe, A., 1984, Rational Krylov sequence methods for eigenvalue computation. *Linear Algebra Appl, 58*, 391–405.
[4] Mallat, S., 1998, A Wavelet Tour of Signal Processing, Academic Press
[5] Weigand, P., Meier, W., Duan, X.R., Stricker, W and Aigner, M., 2006, Investigations of swirl flames in a gas turbine model combustor, I. Flow field, structures, temeperature, and species distribution, Comb. Flame 144, 205-224.
[6] Lewalle, J., Farge, M. and Schneider, K., 2007, Wavelets, in *Springer Handbook of Experimental Fluid Mechanics*, Springer Verlag.
[7] Lammel, O., Geigle, K.-P., Lückerath, R., Meier, W. and Aigner, M., 2007, Investigation of Soot Formation and Oxidation in a High-Pressure Gas Turbine Model Combustor by Laser Techniques, ASME Turbo Expo 2007: Power for Land, Sea and Air, May 14-17, 2007, Montreal (Canada), doi 10.1115/GT2007-27902
[8] Rowley, C.W., Mezic, I., Bagheri, S., Schlatter, P. and Henningson, D.S., 2009, Spectral analysis of nonlinear flows, J. Fluid Mech., 641, 115-127.
[9] Schmid, P., 2010, Dynamic mode decomposition of numerical and experimental data, J. Fluids Eng., 132, 031201/1-13.
[10] Geigle, K.-P., Zerbs, J., Köhler, M., Stöhr, M. and Meier, W., 2011, Experimental Analysis of Soot Formation and Oxidation in a Gas Turbine Model Combustor Using Laser Diagnostics, J. Eng. Gas Turbines Power 133 (12), 121503-1 – 121503-9, 2011, doi 10.1115/1.4004154
[11] Boxx, I., Stöhr, M., Carter, C. and Meier, W., 2010, Temporally resolved planar measurements of transient phenomena in a partially-premixed swirl flame in a gas turbine model combustor, Comb. Flame 157, 1510–1525.
[12] Luginsland, T. and Kleiser, L., 2012, Dynamic mode decomposition for swirling jet flows undergoing vortex breakdown, Proc. Appl. Math. Mech., 12, 495-496.
[13] Boxx, I., Slabaugh, C., Kutne, P., Lucht, R.P. and Meier, W., 2014, 3 kHz PIV/OH-PLIF measurements in a gas turbine combustor at elevated pressure, Proc. Combust. Inst. 35, 3793–3802.
[14] Geigle, K.P., Hadef, R., and Meier. W., 2014, "Soot Formation and flame characterization of an aero-engine model combustor burning ethylene at elevated pressure," J. Eng. Gas Turbines Power 136, 021505.
[15] Geigle, K.P., Köhler, M., O'Loughlin,W., and Meier, W., 2015, "Investigation of soot formation in pressurized swirl flames by laser measurements of temperature, flame structures and soot concentrations," Proc. Comb. Inst. 35, 3373-3380.
[16] Boxx, I.G., Carter, C.D., Geigle, K.-P., and Meier W., 2016, "Measurements of Turbulent Swirl Flame Dynamics in an Ethylene-fuelled Gas Turbine Model Combustor at Elevated Pressure," 54th AIAA Aerospace Sciences Meeting, AIAA SciTech Forum, AIAA 2016-0435.
[17] Boxx, I.G., Carter, C.D., Geigle, K.-P., and Meier W., 2016, " Effects of Air Staging on the Dynamics of an Ethylene-fueled Gas Turbine Model Combustor at Elevated Pressure," 18th International Symposium on the Application of Laser and Imaging Techniques to Fluid Mechanics. Lisbon, Portugal. July 4 – 7, 2016.
[18] Alekseenko, S.V., Dulin, V.M., Tookarev M.P. and Markovich, D.M., 2016, A swirling jet with vortex breakdown: three-dimensional coherent structures, Thermophys. Aeromech., 23/2, 301-304.
[19] Slabaugh, C.D., Boxx, I., Werner, S., Lucht, R.P. and Meier, W., 2016. Temporally-Resolved Measurements of the Structure and Dynamics in Partially-Premixed Swirl Flames at Elevated Power Density, AIAA Journal, 54:3, 946-961.
[20] Markovich, D.M., Dulin, V.M., Abdurakipov, S.S., Kozinkin, L.A., Tokarev M.P. and Hanjalic, K., 2016, Helical modes in low- and high-swirl jets measured by tomographic PIV, J. Turb., 17/7, 678-698.

[21] Kan, P., Ruscher, C.J, Lewalle, J. and Gogineni, S., 2017, Near-field shock/shear-layer interactions in simulated three-stream supersonic rectangular jet, in press, AIAA J.
[22] Boxx, I., Geigle, K.-P., Carter, C.D., Lewalle J. and Akih-Kumgeh, B., 2017, Self-induced transition between stable and termoacoustically excited states in a gas turbine combustor, paper 2017-1102, SciTech 2017, Dallas TX, Jan. 9-13 2017
[23] Boxx, I., Carter, C.D., Geigle, K.-P., Maier, W., Akih-Kumgeh, B. and Lewalle, J., 2017, A study of transition in swirl-stabilized flames, ASME-IGTI 2017, paper 64438.